Investigations about the modelling of acoustic properties of periodic porous materials with the shift cell approach

Computation of dispersion diagrams for periodic porous materials modeled as equivalent fluids

Dario Magliacano[a,b,*], Morvan Ouisse[a], Abdelkrim Khelif[a], Sergio De Rosa[b], Francesco Franco[b], Noureddine Atalla[c], Manuel Collet[d]

[a] *FEMTO-ST Institute / Dep. of Applied Mechanics, Univ. Bourgogne Franche-Comté, CNRS/UFC/ENSMM/UTBM, Besançon, 25000, France*
[b] *Dep. of Industrial Engineering, Università di Napoli "Federico II", Corso Umberto I 40, Napoli, 80138, Italy*
[c] *Université de Sherbrooke, 2500 boul. de l'Université, Sherbrooke, J1K 2R1, Québec, Canada*
[d] *École Centrale de Lyon, 36 avenue Guy de Collongue, Écully, 69134, France*

Abstract

The application of shift cell technique is presented and discussed for periodic porous media described with equivalent fluid models: it consists in a reformulation of classical Floquet-Bloch (F-B) conditions, in which the phase shift of the boundary conditions related to wave propagation is integrated into the partial derivative operator; consequently, the periodicity is included in the overall behavior of the structure, while continuity conditions are imposed at the edges of the unit cell. Its major advantage stands in allowing the introduction of any frequency dependence of porous material behavior, through the resolution a quadratic eigenvalue problem, providing an efficient way to compute the dispersion curves of a porous material modeled as an equivalent fluid. A validation and a computational cost comparison are performed between the shift cell technique and the classical F-B approach, pointing out that the first can provide, among its other advantages, a sensible computational time reduction for this kind of analyses. The derivation of the equivalent acoustic properties of the unit cell from its dispersion characteristics is also investigated; indeed, it could be a very efficient approach for designing a sound package by only involving a simple eigenvalue analysis.

*Corresponding author
Email address: dario.magliacano@univ-fcomte.fr, dario.magliacano@unina.it (Dario Magliacano)

To this aim, group velocity matrix formulation and a branch-tracking algorithm are described. Some test cases are used for validating the proposed methodology.

Keywords: vibroacoustics, porous material, shift cell, branch tracking, dispersion diagram, transmission loss

---

List of symbols

c_0	sound speed in the interstitial fluid
C_g	group velocity
d	thickness
E	total energy
E_k	kinetic energy
E_p	potential energy
I	flow of energy
j	imaginary unit
K	bulk modulus
k	wave number in the material
k_0	wave number in the interstitial fluid
m	mass
p	pressure
p^*	conj(p)
p_0	amplitude of the incident pressure
S	surface interested by incident pressure
s	side length
v	instantaneous local velocity
v_E	energy transport speed
x, y, z	space variables
Z_0	characteristic impedance of the interstitial fluid
Z_c	characteristic impedance of the material
Z_s	surface impedance of the material
Γ	domain boundary
θ, ϕ	angles of incidence

ρ	density of the material
ρ_0	density of the interstitial fluid
τ_∞	transmission coefficient
Ω	poro-elastic volume
ω	angular frequency

1. Introduction

The inclusion of vibroacoustic treatments at early stage of product development, through the use of porous media with periodic inclusions, is a powerful strategy for the achievement of lightweight sound packages and represents a convenient solution for manufacturing aspects.

The main advantage of designing sound packages with periodic arrangements is that they can provide a combination of absorption effects, resonance effects and wave interference effects. These configurations can address different applications in transportation (aeronautics, space, automotive, railway), energy and civil engineering sectors, where both weight and space, as well as vibroacoustic integrity and comfort, still remain as critical issues. Indeed, although porous materials are commonly used for vibroacoustic applications, they suffer from a lack of absorption at low frequencies compared to their efficiency at higher ones; this difficulty is usually overcome by multi-layering [1]. However, while reducing the impedance mismatch at the air-material interface, the efficiency of such devices relies on the allowable thickness [2].

A more efficient way to enhance the low frequency performances of sound packages consists in embedding periodic inclusions in a porous layer [3] in order to create wave interferences or resonance effects that may play a positive role in the dynamics of the system.

The classical approach, known as Floquet-Bloch (F-B) theory, provides a strategy to analyze the behavior of systems with a periodic structure. Floquet's seminal paper deals with the solution of 1D partial differential equations with periodic coefficients [4]; in solid state physics, Bloch generalizes Floquet's results to 3D systems and obtains the description of the wave function associated with an electron traveling across a periodic crystal lattice [5]. This wave function is a solution of the Schrödinger equation with a periodic potential and Bloch showed that it is the product of a simple plane wave multiplied by a periodic function with the same lattice periodicity. In the literature dealing with wave propagation problems in mechanical systems, the theory is referred to as Floquet-Bloch theory [4].

In layered systems, due to the heterogeneity of the relevant elastic properties or to particular geometric features, or to both, only certain wave modes can physically propagate inside the structure. Each of these modes can be identified by a determined (generally nonlinear) function relating the time frequency and the spatial frequency (or wave number). These relationships are called dispersion curves and they summarize all the dynamic behavior of the system [4]. Therefore, dispersion curves offer a better perspective to explain the wave field behavior inside bodies.

For instance, the Helmholtz equation is a known example of equation describing the spatial behavior: there, the physical periodic structure of the studied object translates into spatial periodicity of its coefficients. Therefore, the F-B theory can be applied to obtain the dispersive properties of different mechanical periodic systems, reducing the problem to the calculations performed in the so-called unit cell under to certain specific boundary conditions derived from the F-B theory itself [6].

In order to develop efficient numerical techniques to handle the problem, the shift cell operator technique is presented in Section 2. It allows the description of the propagation of all existing waves from the description of the unit cell through the resolution of a quadratic eigenvalue problem. This is done through a $k(\omega)$ (wave number as a function of the angular frequency) method, that allows computing dispersion curves for frequency-dependent problems, instead of using the classical $\omega(k)$ (angular frequency as a function of wave number) that leads to non-linear eigenvalue problems.

Similar techniques, which use a modified F-B approach in order to handle a $k(\omega)$ problem, can be found in literature ([7, 8, 9]). The main reason why the shift cell method differs from them is that it consists in a reformulation of classical F-B conditions, in which the phase shift of the boundary conditions related to wave propagation is integrated into the partial derivative operator; consequently, the periodicity is included in the overall behavior of the structure, while continuity conditions are imposed at the edges of the unit cell. This hence avoids condensation or non-linear eigenvalue solver, which are required by other approaches. This technique has been successfully applied for describing the mechanical behavior of periodic structures embedding visco-elastic materials ([10, 11]) or piezoelectric materials ([12, 13]). Here it is proposed an extension to equivalent fluid models of porous materials: this makes possible to overcome the limits of existing approaches by a more specific design of the system, through a process of optimization and testing of different inclusions, in order to obtain a device whose frequency efficiency

outperforms existing designs.
After some theoretical background (Section 2), a validation of the shift cell implementation is in Section 3. Dispersion curves, computed along the direction that in a 3D system corresponds to $\phi = 0°$ and $\theta = 0°$ (Figure 1) in the first Brillouin zone [14], are shown in Section 4, while a transmission loss comparison is presented in Section 5; in particular, these results are obtained for a 3D melamine unit cell, with and without inclusion. The behavior of this porous material is described by Johnson-Champoux-Allard (JCA) model [15, 16] in the following sections, but one can identically use any other equivalent fluid model [17, 18, 19].
It is, then, shown that, starting from the complex wave numbers obtained as an output from the quadratic eigenvalue problem, it is possible to compute an equivalent transmission loss curve for an excitation at normal incidence; the comparison with results obtained using classical methods, shows a very good agreement.

2. Shift cell operator technique

In this paper, a periodic arrangement of porous materials is considered. The behavior of each material is described by an equivalent fluid model in the frequency domain, i.e.:

$$\rho \frac{\omega^2}{K} p + \Delta p = 0, \tag{1}$$

where $p = p(\boldsymbol{x}, \omega)$ is the acoustic pressure, $\boldsymbol{x} = (x, y, z)$ is the coordinate vector, ω is the angular frequency, $\rho = \rho(\boldsymbol{x}, \omega)$ is the equivalent fluid density and $K = K(\boldsymbol{x}, \omega)$ is the bulk modulus [20]. The periodicity is described by $\rho(\boldsymbol{x} - \boldsymbol{rn}) - \rho(\boldsymbol{x}) = 0$ and $K(\boldsymbol{x} - \boldsymbol{rn}) - K(\boldsymbol{x}) = 0, \forall \boldsymbol{x} \in \Omega$, where $\boldsymbol{n}$ is a vector of integers normal to the face considered, $\boldsymbol{r} = (\boldsymbol{r}_1, \boldsymbol{r}_2, \boldsymbol{r}_3)$ is a matrix containing the three vectors defining the cell periodicity directions and lengths, and Ω is the domain of interest.
The classical F-B approach, that here is recalled in its 1D formulation but can easily be generalized for 3D applications, provides a strategy to obtain a set of solutions of a linear ordinary equations system. Only the solution inside a period is needed, verifying that

$$\widetilde{\boldsymbol{f}}(x + L) = \rho_F \widetilde{\boldsymbol{f}}(x). \tag{2}$$

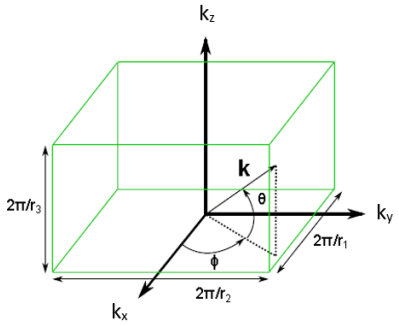

Figure 1: Reciprocal lattice vector in a 3D unitary cell [11].

Following the classical nomenclature, $\rho_F = e^{k_F L}$ is known as Floquet multiplier, k_F being the complex Floquet exponent. Moreover, Floquet found that the solution at any point can also be factorized in two terms:

$$\widetilde{\boldsymbol{f}}(x) = \boldsymbol{p}(x)e^{k_F x}, \tag{3}$$

where $\boldsymbol{p}(x)$ is a periodic function, playing the role of the eigenvectors and carrying the periodicity L of the coefficients of the problem [6]. Any solution of Eq. 1 can therefore be expressed in the form of Eq. 3.

For the purpose of the shift cell technique development, considering Eq. 1 and applying the Bloch theorem such as $p(\boldsymbol{x}, \omega) = p(\boldsymbol{x})e^{j\boldsymbol{k}\boldsymbol{x}}$, where $\boldsymbol{k}$, for a 3D application (Figure 1), is

$$\boldsymbol{k} = k \begin{pmatrix} \cos\theta\cos\phi \\ \cos\theta\sin\phi \\ \sin\theta \end{pmatrix} \tag{4}$$

one can obtain

$$\rho\frac{\omega^2}{K}p + (\nabla + j\boldsymbol{k})^T(\nabla + j\boldsymbol{k})p = 0. \tag{5}$$

$p(x)$ being periodic, the Dirichlet boundary conditions imply $p(L) = p(0)$.

2.1. Weak formulation

The aim of this section is the development of the weak formulation of the problem, in order to obtain a matrix equation that fully describes what happens inside a periodic unit cell of equivalent fluid. A weak formulation

of Eq. 5 consists in finding p such that $\forall \widetilde{p}$, which obeys to the periodic boundary conditions, one has:

$$\omega^2 \int_\Omega \frac{1}{K}\widetilde{p}pd\Omega + \int_\Omega \frac{1}{\rho}\widetilde{p}\nabla^T\nabla pd\Omega + j\boldsymbol{k}\int_\Omega \frac{1}{\rho}\widetilde{p}\nabla^T pd\Omega + j\boldsymbol{k}^T\int_\Omega \frac{1}{\rho}\widetilde{p}\nabla pd\Omega + \\ - \boldsymbol{k}^T\boldsymbol{k}\int_\Omega \frac{1}{\rho}\widetilde{p}pd\Omega = 0. \tag{6}$$

After integrating by parts the second term and considering that Γ is the boundary domain, one obtains

$$\omega^2 \int_\Omega \frac{1}{K}\widetilde{p}pd\Omega + \int_\Gamma \frac{1}{\rho}\widetilde{p}\nabla pd\Gamma - \int_\Omega \frac{1}{\rho}\nabla^T\widetilde{p}\nabla pd\Omega + 2j\boldsymbol{k}\int_\Omega \frac{1}{\rho}\widetilde{p}\nabla pd\Omega + \\ - \boldsymbol{k}^T\boldsymbol{k}\int_\Omega \frac{1}{\rho}\widetilde{p}pd\Omega = 0. \tag{7}$$

The boundary condition causes the integral on the boundary to vanish:

$$\omega^2 \int_\Omega \frac{1}{K}\widetilde{p}pd\Omega - \int_\Omega \frac{1}{\rho}\nabla^T\widetilde{p}\nabla pd\Omega + 2j\boldsymbol{k}\int_\Omega \frac{1}{\rho}\widetilde{p}\nabla pd\Omega - \boldsymbol{k}^T\boldsymbol{k}\int_\Omega \frac{1}{\rho}\widetilde{p}pd\Omega = 0. \tag{8}$$

$$\omega^2 \int_\Omega \frac{1}{K}\widetilde{p}pd\Omega - \int_\Omega \frac{1}{\rho}\nabla^T\widetilde{p}\nabla pd\Omega + j\boldsymbol{k}\int_\Omega \frac{1}{\rho}(\widetilde{p}\nabla p - \nabla\widetilde{p}p)d\Omega + \\ - \boldsymbol{k}^T\boldsymbol{k}\int_\Omega \frac{1}{\rho}\widetilde{p}pd\Omega = 0. \tag{9}$$

Finally, considering that $\boldsymbol{\varphi}$ is the eigenvector, the equation can be written in its matrix form

$$(\boldsymbol{K} + jk\boldsymbol{L} + k^2\boldsymbol{H} - \omega^2\boldsymbol{M})\boldsymbol{\varphi} = 0 \tag{10}$$

with the following matrices:

- $\boldsymbol{K} \propto \int_\Omega \frac{1}{\rho}\nabla\widetilde{p}\nabla pd\Omega$;
- $\boldsymbol{L} \propto \int_\Omega \frac{1}{\rho}(\nabla\widetilde{p}p - \widetilde{p}\nabla p)d\Omega$;
- $\boldsymbol{H} \propto \int_\Omega \frac{1}{\rho}\widetilde{p}pd\Omega$;
- $\boldsymbol{M} \propto \int_\Omega \frac{1}{K}\widetilde{p}pd\Omega$.

Here, $\boldsymbol{M}$ and $\boldsymbol{K}$ are respectively the standard symmetric definite mass and symmetric semi-definite stiffness matrices, $\boldsymbol{L}$ is a skew-symmetric matrix and $\boldsymbol{H}$ is a symmetric semi-definite positive matrix.

2.2. Right and left eigenvalue problems

In this sub-section, the link between right and left eigenvectors is derived. The latter formulation leads to the following right eigenvalue problem:

$$[(\boldsymbol{K} - \omega^2 \boldsymbol{M}) + \lambda_i \boldsymbol{L} - \lambda_i^2 \boldsymbol{H}]\boldsymbol{\varphi}_i^r = 0 \tag{11}$$

where $\lambda_i = jk_i$ is the i-th eigenvalue and φ_i^r denotes the right eigenvector associated to λ_i. In this formulation, all matrices are frequency dependent. The Eq. 11 can be rewritten as

$$\boldsymbol{A}_1(\omega)\boldsymbol{\psi}_i^r = \lambda_i \boldsymbol{A}_2(\omega)\boldsymbol{\psi}_i^r \tag{12}$$

with

- $A_1(\omega) = \begin{pmatrix} 0 & \boldsymbol{I_d} \\ \boldsymbol{K} - \omega^2 \boldsymbol{M} & \boldsymbol{L} \end{pmatrix}$;
- $A_2(\omega) = \begin{pmatrix} \boldsymbol{I_d} & 0 \\ 0 & \boldsymbol{H} \end{pmatrix}$;
- $\boldsymbol{\psi}_i^r = \begin{pmatrix} \boldsymbol{\varphi}_i^r \\ \lambda_i \boldsymbol{\varphi}_i^r \end{pmatrix}$.

where $\boldsymbol{I_d}$ is the identity matrix. Conversely, a left-eigenvector for the same eigenvalue satisfies

$$\boldsymbol{\psi}_i^{l^T} \boldsymbol{A}_1(\omega) = \lambda_i \boldsymbol{\psi}_i^{l^T} \boldsymbol{A}_2(\omega), \text{ with } \boldsymbol{\psi}_i^l = \begin{pmatrix} \boldsymbol{A} \\ \boldsymbol{B} \end{pmatrix}. \tag{13}$$

$$\begin{cases} \boldsymbol{B} = \boldsymbol{\varphi}_{-i}^r = \boldsymbol{\varphi}_i^l \\ \boldsymbol{A}^T = \lambda_i \boldsymbol{\varphi}_{-i}^{r^T} \boldsymbol{H} - \boldsymbol{\varphi}_{-i}^{r^T} \boldsymbol{L} = \lambda_i \boldsymbol{\varphi}_i^{l^T} \boldsymbol{H} - \boldsymbol{\varphi}_i^{l^T} \boldsymbol{L} \end{cases} \tag{14}$$

In the resolution of the right eigenvalue problem, the i-th mode ($i \in N^+$) is defined by its λ_i and its eigenvector $\boldsymbol{\varphi}_i^r$. For each mode i, a mode $-i$ is associated with λ_{-i} such that $\lambda_{-i} = -\lambda_i$ and $\boldsymbol{\varphi}_{-i}^r = \boldsymbol{\varphi}_i^l$. Therefore, by solving the right eigenvalue problem, the left solution is found too [11].

2.3. Group velocity

For frequency-dependent systems, the estimation of the group velocity is not trivial [21]. In order to find its expression, Eq. 12 is now differentiated with respect to ω:

$$\frac{\partial \boldsymbol{A}_1(\omega)}{\partial \omega}\boldsymbol{\psi}_i^r + \boldsymbol{A}_1(\omega)\frac{\partial \boldsymbol{\psi}_i^r}{\partial \omega} = \frac{\partial \lambda_i}{\partial \omega}\boldsymbol{A}_2(\omega)\boldsymbol{\psi}_i^r + \lambda_i\frac{\partial \boldsymbol{A}_2(\omega)}{\partial \omega}\boldsymbol{\psi}_i^r + \lambda_i\boldsymbol{A}_2(\omega)\frac{\partial \boldsymbol{\psi}_i^r}{\partial \omega} \quad (15)$$

and multiplied by the left eigenvector such that:

$$\begin{aligned} &\boldsymbol{\psi}_i^{l^T}\frac{\partial \boldsymbol{A}_1(\omega)}{\partial \omega}\boldsymbol{\psi}_i^r + \boldsymbol{\psi}_i^{l^T}\boldsymbol{A}_1(\omega)\frac{\partial \boldsymbol{\psi}_i^r}{\partial \omega} = \\ &= \boldsymbol{\psi}_i^{l^T}(\frac{\partial \lambda_i}{\partial \omega}\boldsymbol{A}_2(\omega) + \lambda_i\frac{\partial \boldsymbol{A}_2(\omega)}{\partial \omega})\boldsymbol{\psi}_i^r + \boldsymbol{\psi}_i^{l^T}\lambda_i\boldsymbol{A}_2(\omega)\frac{\partial \boldsymbol{\psi}_i^r}{\partial \omega}. \end{aligned} \quad (16)$$

Considering that

$$\boldsymbol{\psi}_i^{l^T}\boldsymbol{A}_1(\omega) = \lambda_i\boldsymbol{\psi}_i^{l^T}\boldsymbol{A}_2(\omega) \quad (17)$$

one obtains

$$\frac{\partial \lambda_i}{\partial \omega} = \frac{\boldsymbol{\psi}_i^{l^T}[\frac{\partial \boldsymbol{A}_1(\omega)}{\partial \omega} - \lambda_i\frac{\partial \boldsymbol{A}_2(\omega)}{\partial \omega}]\boldsymbol{\psi}_i^r}{\boldsymbol{\psi}_i^{l^T}\boldsymbol{A}_2(\omega)\boldsymbol{\psi}_i^r} \quad (18)$$

which gives the expression of the group slowness using $\lambda_i = jk_i$:

$$\frac{\partial k_i}{\partial \omega} = -j\frac{\boldsymbol{\varphi}_i^{l^T}[-2\omega\boldsymbol{M} + \frac{\partial \boldsymbol{K}}{\partial \omega} + \lambda_i\frac{\partial \boldsymbol{L}}{\partial \omega} - \lambda_i^2\frac{\partial \boldsymbol{H}}{\partial \omega}]\boldsymbol{\varphi}_i^r}{\boldsymbol{\varphi}_i^{l^T}[-\boldsymbol{L} + 2\lambda_i\boldsymbol{H}]\boldsymbol{\varphi}_i^r}. \quad (19)$$

Finally, the complex group velocity is the inverse of the complex group slowness [21]:

$$C_g = \frac{\partial \omega}{\partial k_i} = \frac{j\boldsymbol{\varphi}_i^{l^T}[-\boldsymbol{L} + 2\lambda_i\boldsymbol{H}]\boldsymbol{\varphi}_i^r}{\boldsymbol{\varphi}_i^{l^T}[-2\omega\boldsymbol{M} + \frac{\partial \boldsymbol{K}}{\partial \omega} + \lambda_i\frac{\partial \boldsymbol{L}}{\partial \omega} - \lambda_i^2\frac{\partial \boldsymbol{H}}{\partial \omega}]\boldsymbol{\varphi}_i^r}. \quad (20)$$

It should be noted that the frequency dependence of porous material models is generally known analytically, hence the computation of C_g is fast since the derivatives of the matrices with respect to ω can be expressed analytically.

2.4. Classifying criteria to distinguish propagative and evanescent waves

When the shift cell operator technique is applied to a sample modeled through an equivalent fluid, all wave numbers are complex; consequently, there is no purely propagative solution and all waves are damped, with a decay rate that may be used to classify the branches in two categories: those that are rapidly damped and those that are slowly damped in space. Hence, the latter could be classified as "propagative" ones.
In general, the distinction between them is difficult and, thus, two classifying criteria are proposed.

1. The ratio between the real and the imaginary parts of every wave number [11]: $C_1 = \frac{real(k)}{imag(k)}$. The physical meaning of C_1 is related to the fact that the real part of a wave number represents the propagative behavior, while its imaginary part is linked to the dissipation and therefore should be smaller than the real part in order to be able to consider a wave as propagative. It should be pointed out that, since the real part of k is periodic while the imaginary one is not, in order to correctly apply this criterion the real part of k must be turned into non-periodic, by mirroring it in correspondence to each period.
2. The ratio between the real part of the energy transport speed, defined as $v_E = \frac{I}{E}$ for undamped waves, and the real part of group velocity C_g: $C_2 = \frac{real(v_E)}{real(C_g)}$, where I is the flow of energy and $E = E_k + E_p = \int_\Omega \frac{1}{2}(\rho v^2 + \frac{p^2}{\rho c^2}) d\Omega$ is the total energy. Waves may be qualified as propagative when the energy is transported at a velocity which is at least close to the order of the group velocity.

Only the waves corresponding to $C_1 > \tau_1$ and $C_2 > \tau_2$ are considered as propagative ones. In practice, for the purpose of the following analysis, the thresholds τ are chosen such as $\tau_1 = 1$ and $\tau_2 = 0.7$.
These thresholds may be chosen differently according to the problem of interest [11]. Since there is no strict distinction between "propagative" and "evanescent" waves, an alternative would be to define an indicator of the "propagativeness" nature for each (ω, k) value of the dispersion diagram.
This is illustrated later in the results presented in Section 4.

3. Validation of the method

3.1. Analysis of undamped case

In order to validate the implementation, a first calculation is made to compare shift cell results with those obtained using classical F-B periodic conditions, using (non-dissipative) air as material. Both methods are used to obtain the dispersion diagram along the direction that corresponds to $\phi = 0°$ and $\theta = 0°$ (for the 3D case) in the first Brillouin zone.
The only non-null component of the wave vector is then the first one and $k = k_x$. The parameters used for air are: $\rho_{air} = 1.2050\frac{kg}{m^3}$ (density), $c_{air} = 343.2886\frac{m}{s}$ (speed of sound) and $K_{air} = 142kPa$ (bulk modulus). A perfectly rigid cylindrical inclusion is located at the center of the unit cell and its geometric data are reported in details in Sub-section 4.2. The comparison shows a perfect agreement between the results of the two methods (Figure 2). In particular, one can observe that this arrangement exhibits a band gap between 6000 Hz and 10000 Hz for waves propagating along x direction.

3.2. Meaning and behavior of band gaps for inclusions of increasing size

Figure 3 shows on the left what happens to the band gap, in the previously defined 2D unit cell, when the size of the inclusion (that has perfectly rigid walls) changes. The radius of the inclusion for the three analyzed cases are respectively equal to $\frac{s}{32}$, $\frac{s}{4}$ and $\frac{s}{2.1}$, where s is the side length: the opening frequency of the Bragg band gap decreases when the radius is increased, and at the same time the width of the gap is increasing.
In the previous sub-section, only the real part of the wave number is shown. Now both real and imaginary parts are shown, while no damping is included in the model: k is either purely real, the wave is then propagative, or purely imaginary, the wave being then evanescent.
After this, instead of using the adiabatic value (142 kPa) for the bulk modulus of air, one can artificially add a frequency-constant imaginary part to it ($142 + j12$ kPa is used here for illustration), so that one can simulate a band gap behavior in presence of hysteretic dissipation. The new dispersion curves are shown on the right of Figure 3. Indeed, a complex bulk modulus prevents the presence of perfect band gaps in dispersion curves; one can clearly see that the gap is opening but, because of the damping, k_x is no longer purely imaginary. So, the real part of k_x does not cancel anymore, but remains low (compared to imaginary one), which means that the wave will be strongly spatially attenuated.

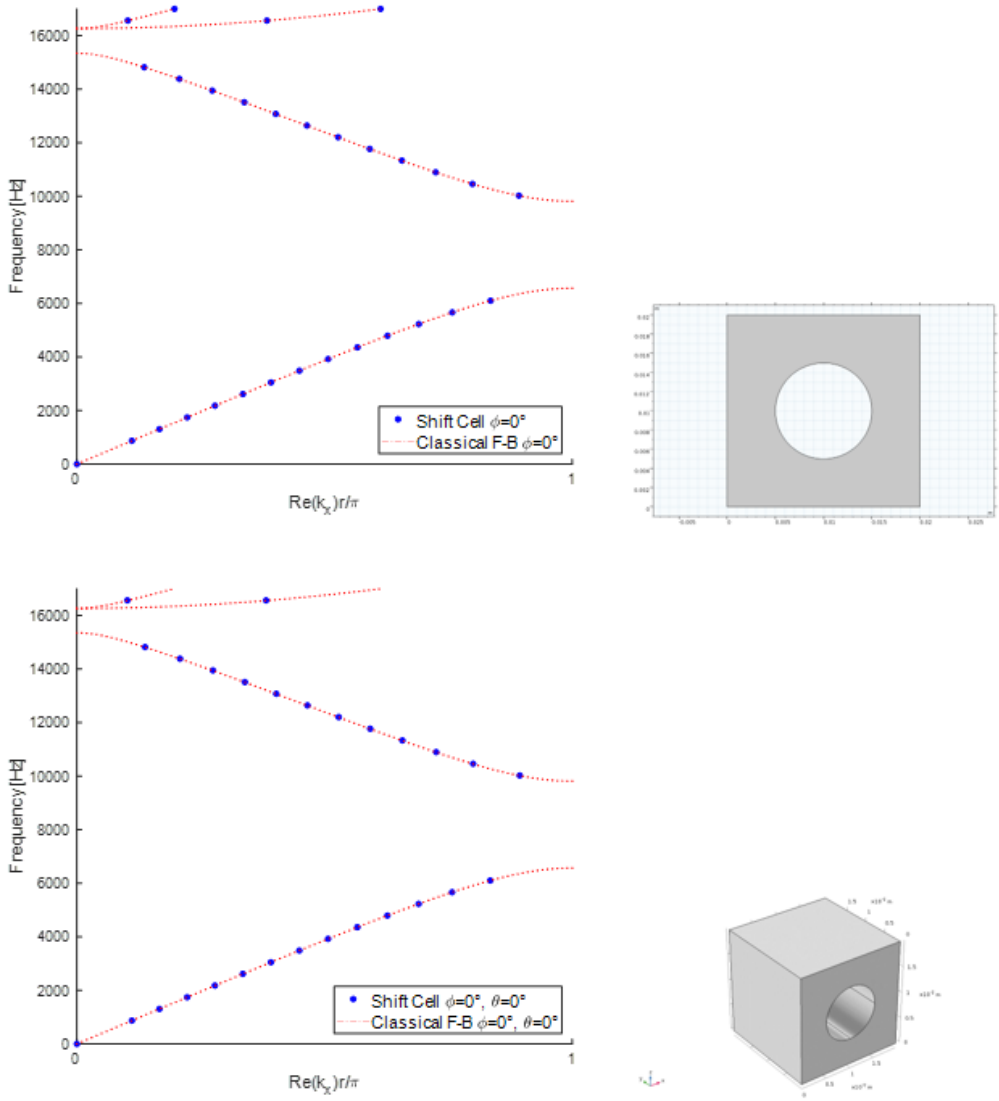

Figure 2: Comparison between dispersion curves obtained with classical Floquet-Bloch and shift cell techniques on a 2D (on the top) and a 3D (on the bottom) air unit cell. Stepped red lines: classical F-B method; blue points: shift cell operator.

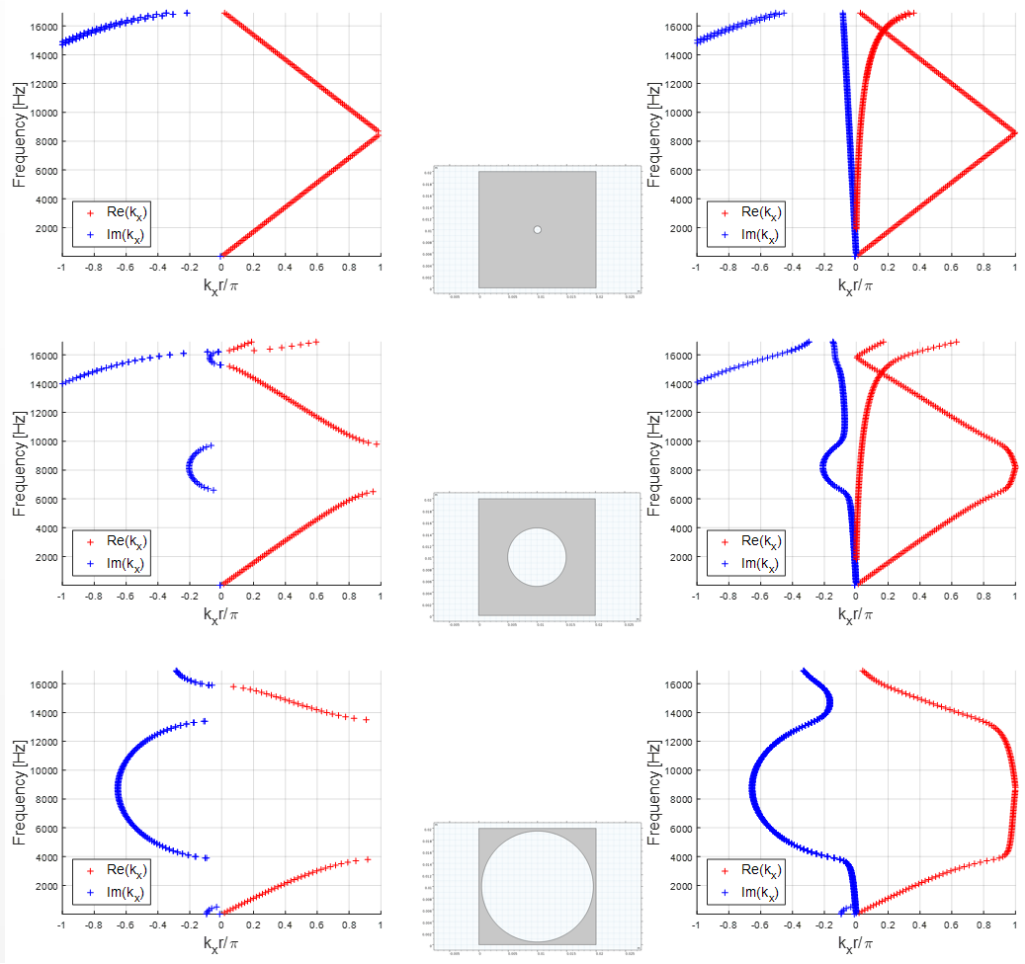

Figure 3: Dispersion curves for an air 2D cell, with increasing inclusion size (from top to bottom), with adiabatic (first column) and complex (second column) bulk modulus.

Also, a very fast branch can be observed in the two first cases: around the band gap, the slow branch with undamped material becomes a fast wave when damping is added and allows rapid and damped energy transportation inside the band gap.

3.3. Comparison of computational cost

It is now performed a computational cost comparison between the shift cell technique and the classical F-B approach, pointing out that the first can provide, among its other advantages, a sensible computational time reduction for dispersion analyses. Figure 4 and Figure 5 show a comparison of the computational cost, in terms of time and as a function of the mesh size, between the shift cell and the F-B techniques. In particular, for both eigenproblems, the COMSOL PARDISO solver is adopted, using 100 frequency steps and 5 requested values; the 2D unit cell is meshed using triangular elements while, for the 3D geometry, tetrahedral elements are used. Both 2D and 3D geometries correspond to those shown in the previous sections and these results, in terms of computational times, are related to an undamped case.
As a conclusion, for the case of interest, the calculation cost is always lower with the proposed approach than the one required by the classical Floquet-Bloch technique.
The gain is increasing when the number of elements of the finite element model is increasing, which makes the technique attractive. The lower cost is attributed to the management of the boundary conditions, which is much more simple in the proposed methodology.

4. Dispersion curves

4.1. Branch-tracking algorithm

In a dispersion diagram there is a set of points, forming branches, that one may wish to connect and follow according to the nature of each branch. Some solutions are proposed in literature, such as a MAC sorting criterion [10], but these methods require to store many data at every iteration. Instead, the group velocity constitutes a relevant indicator in order to follow the branches from a point of calculation to the next one [11]. The proposed technique consists in comparing a single group velocity value at a specific frequency $C_{g_i}(f)$ with $\boldsymbol{C}_{\mathbf{g}}(f + \Delta f)$: from the group velocity associated to a starting point, the routine compares the initial C_{g_i} with all the group velocities at the next frequency step $f + \Delta f$ and a minimization is made in order

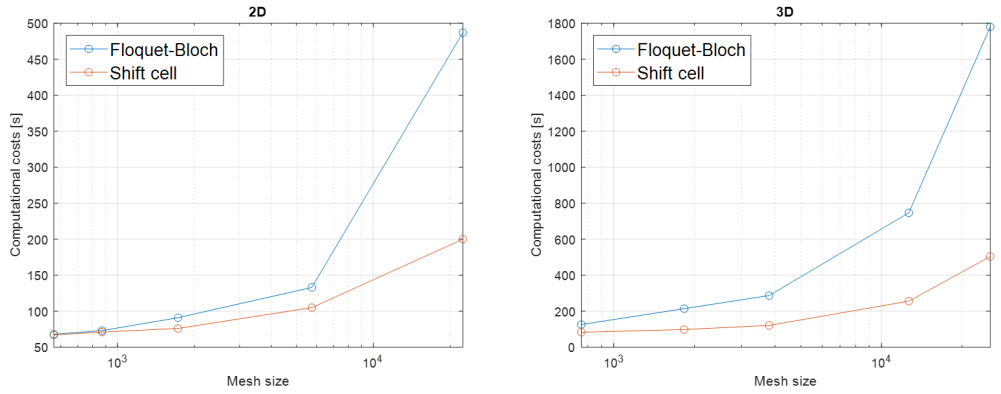

Figure 4: Computational times [s] in the 2D (left) and 3D (right) cases, for increasing number of elements.

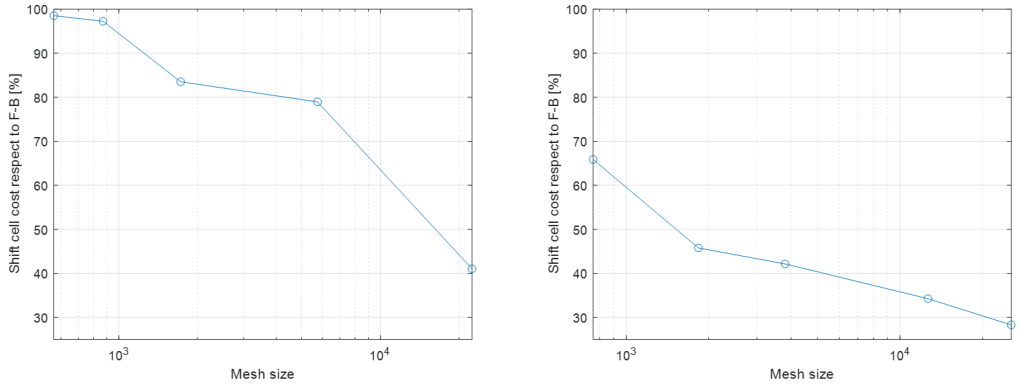

Figure 5: Computational time percentage in the 2D (left) and 3D (right) cases, for increasing number of elements.

to identify the point at $f + \Delta f$ to which is associated the closest value of C_g. Then, this point is defined as the new starting one and so on, step by step, the branch is identified. In order to better appreciate the behavior of each branch in the frequency range of study, in the following plots, dispersion and C_g curves are also colorized with a scale of colors that indicates the level of "propagativeness": the value 0 means that the wave at that specific frequency is totally spatially attenuated, while the value 1 represents a properly propagative behavior. In particular, considering the criteria discussed in Sub-section 2.4, if all of them are satisfied then the propagativeness value is equal to 1, otherwise it is calculated as the product between the results of the two classifying ratios divided by the correspondent thresholds. It should be pointed out that, if a specific criterion is satisfied, its contribution to the estimation of the level of propagativeness is always equal to 1, even if its related ratio is larger. In other words:

$$\text{if } C_1 > \tau_1 \Rightarrow prop_1 = 1, \text{ else } prop_1 = \frac{C_1}{\tau_1} \tag{21}$$

$$\text{if } C_2 > \tau_2 \Rightarrow prop_2 = 1, \text{ else } prop_2 = \frac{C_2}{\tau_2} \tag{22}$$

$$level\ of\ propagativeness = prop_1 \bullet prop_2 \tag{23}$$

In the next Section, for a 3D melamine unit cell, some results are shown in terms of evanescent — propagative dispersion and group velocity diagrams and branch-tracked dispersion and group velocity diagrams. These curves are obtained for both a homogeneous and a heterogeneous (with inclusion) 3D unit cell, whose porous material is modeled with JCA model ([15, 16]).

4.2. Results

Herein, all results are related to a 3D melamine unit cell constituted by a cube with side equal to 2 cm (homogeneous case) and with a 0.5 cm radius cylindrical rigid inclusion (case with inclusion). The analyses are carried out in the frequency range 0 – 17000 Hz.

This range, indeed, is interesting for acoustic applications and assures that the wavelength is much larger than the pore size, which is a necessary condition in order to use equivalent fluid models. The size of the inclusion is also large compared to the typical characteristic length that may be observed on a representative elementary volume describing the macroscopic behavior of the porous material [22].

Porosity	0.99
Tortuosity	1.02
Resistivity $[\frac{Pa \times s}{m^2}]$	8430
Viscous char. length $[mm]$	0.138
Termal char. length $[mm]$	0.154

Table 1: Acoustical parameters of the tested porous material.

It is well known that the parameters of the equivalent fluid models can have a strong impact on the performances of the acoustic device [23], hence they should be determined in a confident way. In the current case, they have been experimentally determined and are reported in Table 1. In Figures 6 and 7, the two plots on the top and the center of each figure represent two different ways to show the classification between evanescent and propagative waves: on the top, the plot is directly obtained from the application of the criteria presented in Sub-section 2.4, while on the center the same distinction is shown using a color scale of "propagativeness" as described in Section 4.1. For each dispersion curve, three eigenvectors are reported (Figures 8 and 9). Only the real parts are shown, the imaginary parts being null. They are all extracted at the frequency of 8500 Hz and along the direction that corresponds to $\theta = \phi = 0°$ in the first Brillouin zone. Their branches are ordered as follows: at increasing frequencies, the 1st branch is represented by the first real part that reaches the unitary value, the 2nd one is the second that satisfies this condition and so on.
For what concerns the propagative – evanescent plots, one can notice that the first mode propagates at almost all frequencies, the second one appears to be propagative starting from middle frequencies, while the third and fourth ones are relevant only at high frequencies. The branch-tracking algorithm is quite robust and works well even in presence of band gaps, branch-crossing or branch-veering phenomena.

5. Computation of transmission loss from dispersion diagrams

Dispersion diagrams presented above help designers to understand the nature of the waves that can propagate in a sound package and the way they are attenuated on the basis of an infinite periodic arrangement of the unit cell. In this section, it is shown how these results can be used to estimate the transmission loss at normal incidence for an acoustic package composed

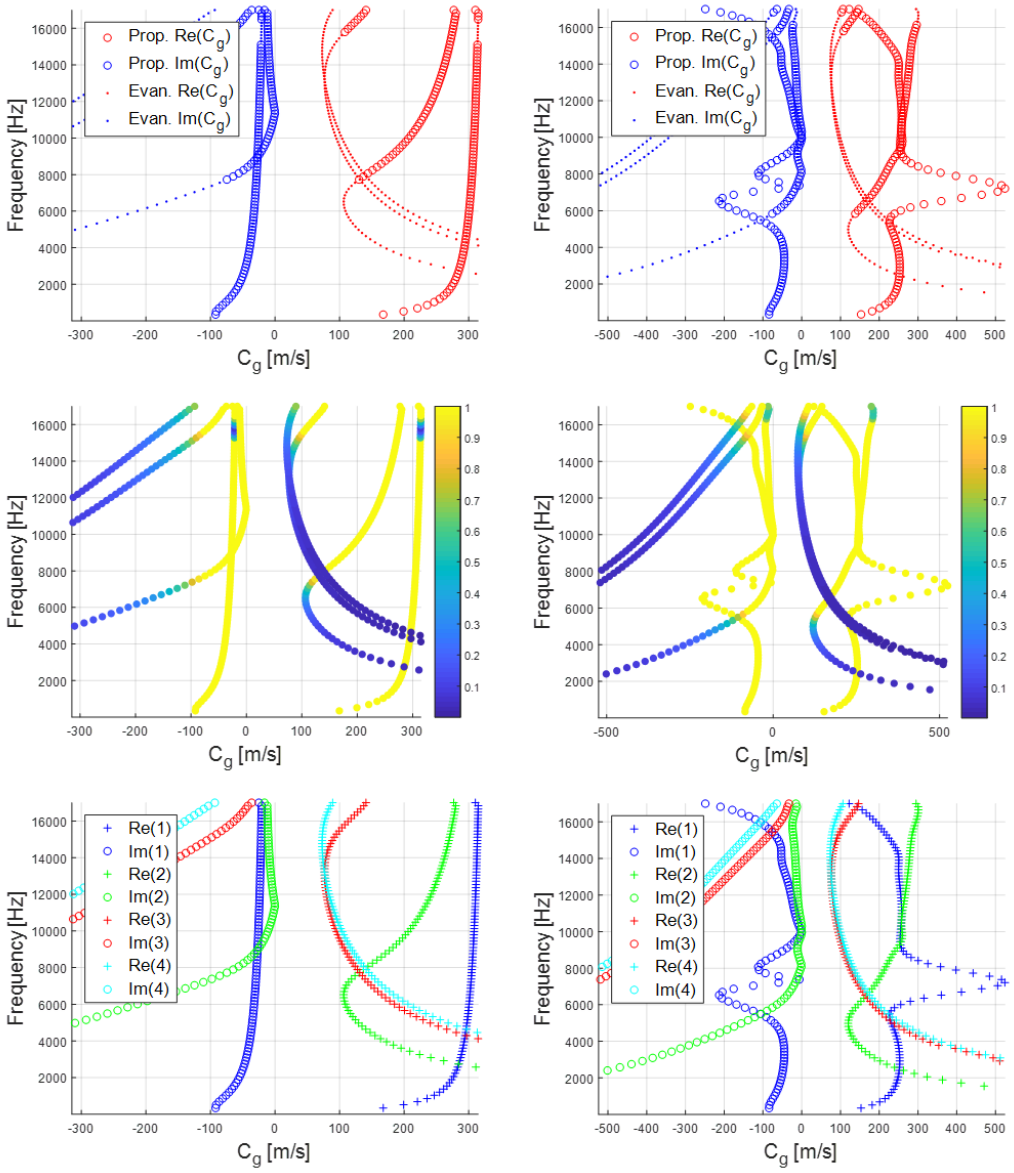

Figure 6: Evanescent and propagative (on the top and the center, in which the color scale indicates the level of propagativeness) and branch-tracked (on the bottom) group velocity diagrams, for the case of a melamine unit cell, homogeneous (on the left) and with a rigid inclusion (on the right). The positive range of the x axis shows the real parts, while its negative zone shows the imaginary ones.

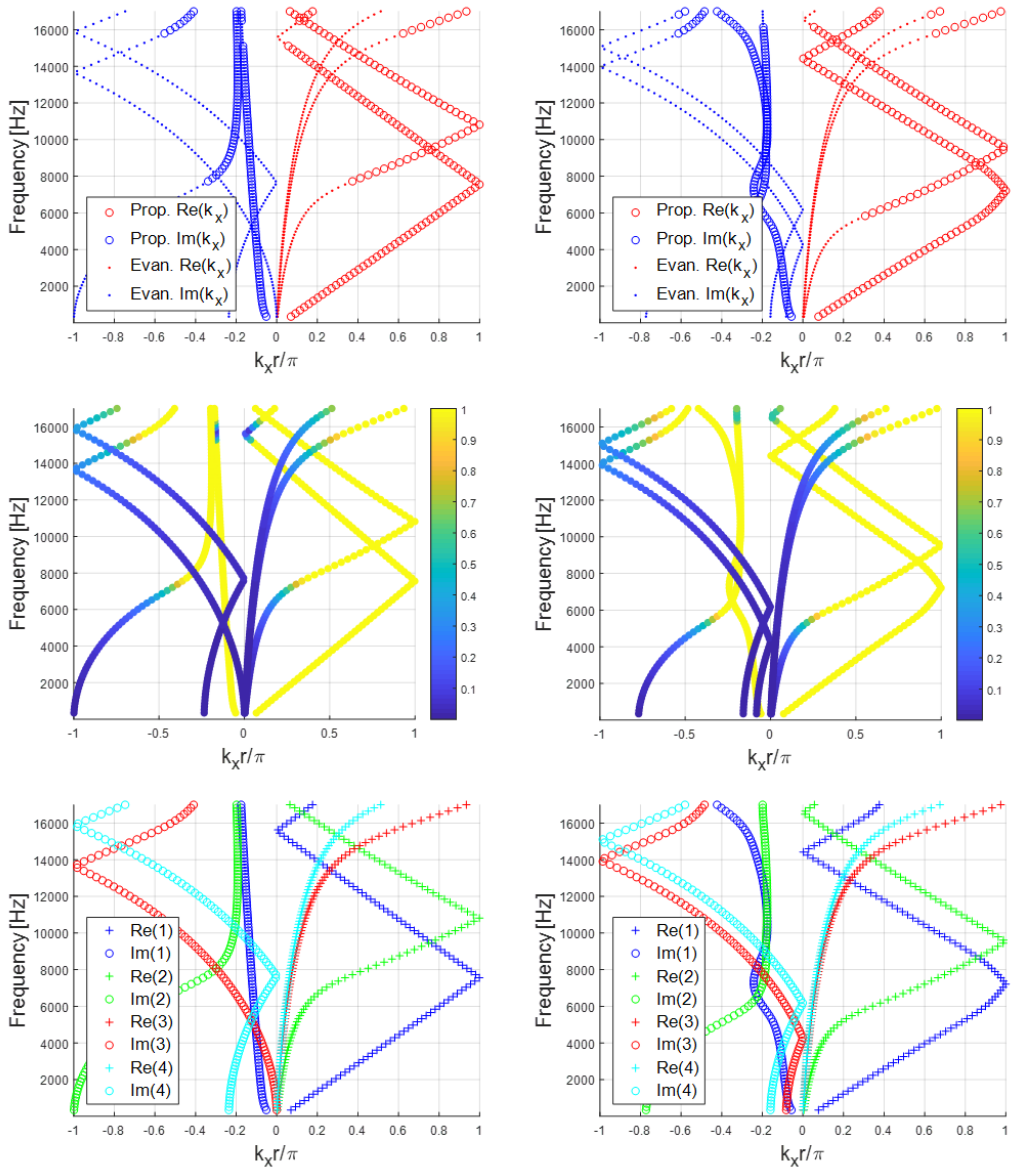

Figure 7: Evanescent and propagative (on the top and the center, in which the color scale indicates the level of propagativeness) and branch-tracked (on the bottom) dispersion diagrams, for the case of a melamine unit cell, homogeneous (on the left) and with a rigid inclusion (on the right). The positive range of the x axis shows the real parts, while its negative zone shows the imaginary ones.

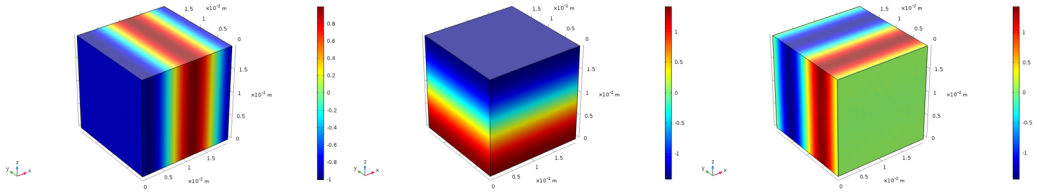

Figure 8: From left to right, real parts of the 1st, 2nd and 3rd branch eigenvectors for a melamine homogeneous unit cell.

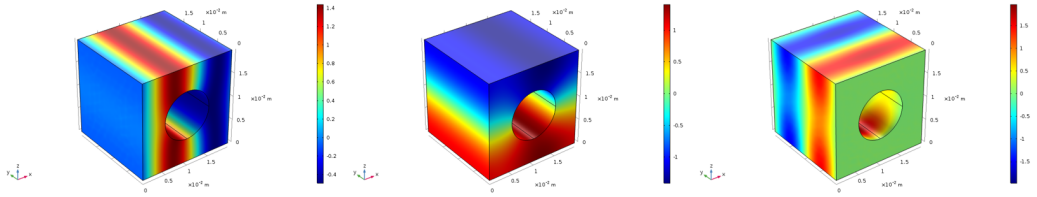

Figure 9: From left to right, real parts of the 1st, 2nd and 3rd branch eigenvectors for a melamine unit cell with a rigid inclusion.

by a finite arrangement of 5 cells. This, in a first approximation, allows comparing the dispersion relations and the acoustical characteristics of the equivalent finite medium. For more complex cases, advanced homogenization techniques may be used [24, 25].

For a plane wave configuration, the transmission loss is computed in three different ways.

I) Transfer matrix method [1] (homogeneous case):

$$TL = 10log_{10}(\frac{1}{4}|T_{11} + \frac{T_{12}}{\rho_0 c_0} + \rho_0 c_0 T_{21} + T_{22}|^2), \tag{24}$$

$$\text{with } \begin{bmatrix} T_{11} & T_{12} \\ T_{21} & T_{22} \end{bmatrix} = \begin{bmatrix} \cos(kd) & j\sin(kd)Z_0 \\ \frac{j\sin(kd)}{Z_0} & \cos(kd) \end{bmatrix}. \tag{25}$$

II) Full FEM with 5 cells (case with inclusion):

$$TL = 10log_{10}\frac{\Pi_{incident}}{\Pi_{transmitted}} \tag{26}$$

where $\Pi_{incident}$ and $\Pi_{transmitted}$ represent the incident and transmitted power, respectively. For this configuration, the calculation is made

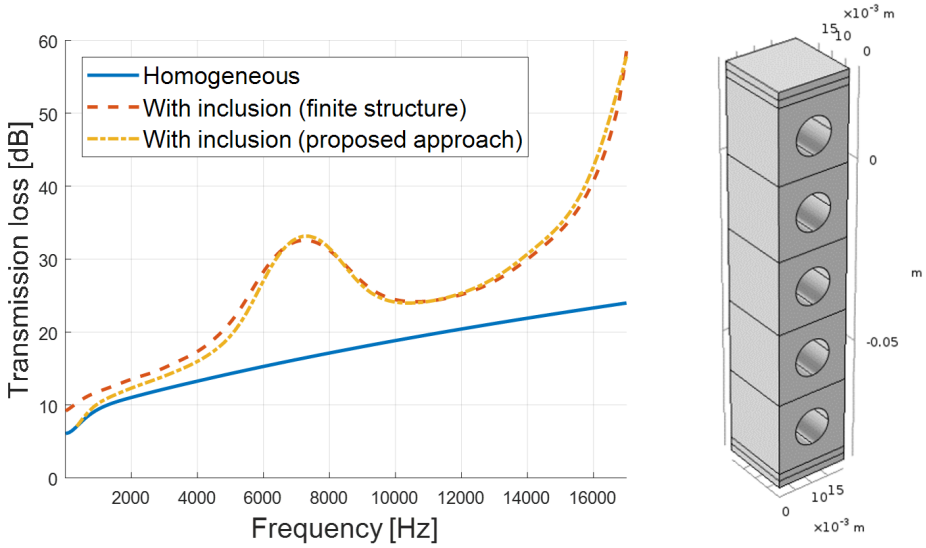

Figure 10: Transmission loss computed for a 3D repetition of 5 melamine unit cells.

using an implementation of the plane wave forced response of the periodic cell accounting for fluid loading [26].

III) Transfer matrix method with 5 cells, where k is provided by the dispersion curves (proposed approach); in order to perform this estimation, only the first branch of the diagram is taken into account, since it is the only one to which corresponds an eigenvector along the direction of the plane wave excitation.

Concerning the case with the inclusion, one can notice that an improvement of transmission loss properties, with respect to the homogeneous case, is shown at all frequencies, in particular in correspondence of a peak at a frequency around 7 kHz, where a gain of about 15 dB is observed, and at high frequencies.

Note that, for the sake of comparison with the related dispersion curves, only their 1^{st} branch is meaningful due to the fact that the corresponding mode is the only one that is actually excited during these transmission loss simulations.

Indeed, the TL improvement peak exactly corresponds to the frequency range of the 1^{st} branch of dispersion curves in which the wave is strongly spatially attenuated. This is definitely encouraging, for the purpose of deriving the equivalent acoustic properties of the unit cell from its dispersion characteris-

tics.

6. Conclusions

In this paper, the formulation of the shift cell technique is presented together with some applications aimed at evaluating the dispersive properties of some foams modeled as a periodic porous medium. The benefit of the $k(\omega)$ formulation, in the extraction of the problem eigenvalues, is shown and commented.

Since the numerical formulation for the foams leads all complex wave numbers, one of the key elements of the present research activities is the definition of adequate classifying criteria. As matter of fact, there is no purely propagative solution and all waves are damped, with a decay rate that may be used to classify the branches in two categories: those that are rapidly damped and those that are slowly damped in space. The proposed criteria allow to distinguish between the evanescent and propagative waves traveling in the material and, consequently, to derive the group velocity.

The proposed technique is validated through a comparison with the application of the classical Floquet-Bloch periodic conditions; these results are related to a melamine unit cell. It is also evidenced a remarkable reduction of the computational costs associated with the application of this shift-cell technique.

Furthermore, thanks to a branch-tracking algorithm, it is possible to compute equivalent transmission loss curves, which show a very good agreement with those obtained with classical methods. The transmission loss results give also some guidelines to tailor a porous medium to specific structural-acoustic requirements.

All results are based on an equivalent fluid model of the analyzed foams. The successive steps of this research work are going to involve the Biot model [27] for 2D and 3D geometries in a solution framework based again on the shift cell technique. The use of the Biot model can allow the definition of an optimized unit cell configuration (involving as parameters the geometry, the materials of the foam and the inclusion).

Acknowledgments

This project has received funding from the European Union's Horizon 2020 research and innovation program under the Marie Skłodowska-Curie

grant agreement No. 675441. It has been performed in collaboration with EUR EIPHI program (ANR 17-EUR-0002).

References

[1] J. F. Allard, N. Atalla, Propagation of sound in porous media: Modelling sound absorbing materials, 2^{nd} Edition, Wiley, 2009.

[2] T. Weisser, J.-P. Groby, O. Dazel, F. Gaultier, E. Deckers, S. Futatsugi, L. Monteiro, Acoustic behavior of a rigidly backed poroelastic layer with periodic resonant inclusions by a multiple scattering approach, J. Acoust. Soc. Am. 139 (2) (2016) 617–629.

[3] J.-P. Groby, A. Wirgin, L. D. Ryck, W. Lauriks, R. P. Gilbert, Y. S. Xu, Acoustic response of a rigid-frame porous medium plate with a periodic set of inclusions, J. Acoust. Soc. Am. 126 (2) (2009) 685–693.

[4] G. Floquet, Sur les équations différentielles linéaires à coefficients périodiques [On the linear differential equations with periodic coefficients], ann. sci. l'École norm. Supérieure 12 (2) (1881) 43.

[5] F. Bloch, Uber die quantenmechanik der elektronen in kristallgittern [On the quantum mechanics of the electrons in crystal lattices], Z. Phys. 52 (1928) 555–600.

[6] P. G. Garcia, J.-P. Fernandez-Alvarez, Floquet-bloch theory and its application to the dispersion curves of nonperiodic layered systems, Math. Probl. Eng. Math. 2015 (2015) 12.

[7] M. Lewinska, J. van Dommelen, V. Kouznetsova, M. Geers, Towards acoustic metafoams: the enhanced performance of a poroelastic material with local resonators, J. Mech. Phys. Solids (2018) 32.

[8] A. Krushynska, V. Kouznetsova, M. Geers, Visco-elastic effects on wave dispersion in three-phase acoustic metamaterials, J. Mech. Phys. Solids 96 (2016) 29–47.

[9] Y.-F. Wang, Y.-S. Wang, V. Laude, Wave propagation in two-dimensional viscoelastic metamaterials, Physical Review B 92 (2015) 14.

[10] M. Collet, M. Ouisse, M. Ruzzene, M. N. Ichchou, Floquet-bloch decomposition for the computation of dispersion of two-dimensional periodic, damped mechanical systems, Int. J. Solids Struct. 48 (20) (2011) 2837–2848.

[11] K. Billon, Composites periodiques fonctionnels pour l'absorption vibroacoustique large bande [Functional periodic composites for vibroacoustic wide-band absorption], PhD thesis at Université de Franche-Comté, 2017.

[12] M. Ouisse, M. Collet, F. Scarpa, A piezo-shunted kirigami auxetic lattice for adaptive elastic wave filtering, Smart Mat. and Struct. 25 (11) (2016) 29.

[13] M. Collet, M. Ouisse, F. Tateo, Adaptive metacomposites for vibroacoustic control applications, IEEE Sensors Journal 14 (7) (2014) 2145–2152.

[14] L. Brillouin, Les électrons dans les métaux et le classement des ondes de de Broglie correspondantes [Electrons in metals and classification of the corresponding de Broglie waves], Comptes Rendus Hebdomadaires des Séances de l'Académie des Sciences 191 (292) (1930) 377–400.

[15] D. L. Johnson, J. Koplik, R. Dashen, Theory of dynamic permeability and tortuosity in fluid-saturated porous media, J. Fluid Mech. 176 (1) (1987) 379–402.

[16] Y. Champoux, J. F. Allard, Dynamic tortuosity and bulk modulus in air-saturated porous media, J. Appl. Phys. 70 (4) (1991) 1975–1979.

[17] M. E. Delany, E. N. Bazley, Acoustical properties of fibrous absorbent materials, Appl. Acoust. 3 (1969) 105–116.

[18] Y. Miki, Acoustical properties of porous materials-modifications of Delany-Bazley models, J. Acoust. Soc. Jpn. 11 (1) (1990) 19–24.

[19] D. Lafarge, P. Lemarinier, J. F. Allard, V. Tarnow, Dynamic compressibility of air in porous structures at audible frequencies, J. Acoust. Soc. Am. 102 (4) (1997) 1995–2006.

[20] A. Bensoussan, J. L. Lions, G. Papanicolaou, Asymptotic Analysis of Periodic Structures, Elsevier, 1978.

[21] R. Moiseyenko, V. Laude, Material loss influence on the complex band structure and group velocity in phononic crystals, Physical Review B 83 (6) (2011) 1–6.

[22] O. Robin, A. Berry, O. Doutres, N. Atalla, Measurement of the absorption coefficient of sound absorbing materials under a synthesized diffuse acoustic field, J. Acoust. Soc. Am. 136 (1) (2014) 7.

[23] M. Ouisse, M. Ichchou, S. Chedly, M. Collet, On the sensitivity analysis of porous material models, Journal of Sound and Vibration 331 (2012) 5292–5308.

[24] A. Madeo, M. Collet, M. Miniaci, K. Billon, M. Ouisse, P. Neff, Modeling phononic crystals via the weighted relaxed micromorphic model with free and gradient micro-inertia, Journal of Elasticity 130 (59) (2018) 25.

[25] C. Boutin, S. Hans, A. Rallu, On inner resonance in elastic composites - design of media with negative mass or stiffness, J. Acoust. Soc. Am. 134 (6) (2013) 4717–4729.

[26] N. Atalla, NOVAFEM User's guide, Université de Sherbrooke, Sherbrooke (QC, Canada), 2017.

[27] M. Biot, Mechanics of deformation, J. Appl. Physiscs 33 (4) (1962) 1482–1498.